

See discussions, stats, and author profiles for this publication at: <https://www.researchgate.net/publication/263943614>

# Preparation and Photoluminescence of (3C-ZnS)/(2H-ZnS) Superlattice in Mn-doped ZnS Nanoribbons

ARTICLE in THE JOURNAL OF PHYSICAL CHEMISTRY C · OCTOBER 2012

Impact Factor: 4.77 · DOI: 10.1021/jp3084138

CITATIONS

11

READS

20

5 AUTHORS, INCLUDING:



Junfeng Lu

Southeast University (China)

21 PUBLICATIONS 71 CITATIONS

SEE PROFILE



Xianghua Zeng

Yangzhou University

54 PUBLICATIONS 175 CITATIONS

SEE PROFILE



Hongfei Liu

Chinese Academy of Sciences

30 PUBLICATIONS 124 CITATIONS

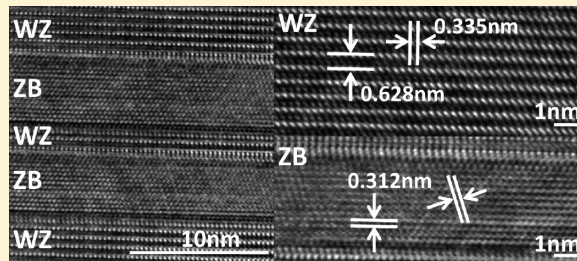
SEE PROFILE

# Preparation and Photoluminescence of (3C-ZnS)/(2H-ZnS) Superlattice in Mn-doped ZnS Nanoribbons

Junfeng Lu, Xianghua Zeng,\* Hongfei Liu, Wei Zhang, and Yong Zhang

College of Physics Science and Technology, Yang Zhou University, Yang Zhou 225002, P.R. China

**ABSTRACT:** In this paper, we report the first successful growth of  $(3\text{C-ZnS})_n/(2\text{H-ZnS})_m$  superlattice structures in Mn-doped ZnS nanoribbons prepared on Au-coated Si substrates by a chemical vapor transport method. The lattice-resolved HRTEM image presents the self-assembled  $(3\text{C-ZnS})(111)/(2\text{H-ZnS})(100)$  superlattices, where both the  $(3\text{C-ZnS})$  ZnS atom layer and the  $(2\text{H-ZnS})$  atom layer are alternately arrayed in the plane of nanoribbons along the axis growth direction. The individual Mn-doped ZnS nanoribbons, with uniform widths ranging from 100 to 800 nm and lengths ranging from tens to one hundred micrometers, are composed of the hexagonal wurtzite atom layers growing along the  $[100]$  axis direction and  $[001]$  vertical direction and the zinc-blende atom layers growing along the  $\langle 111 \rangle$  direction. An identical strong photoluminescence transition peak at 580 nm was observed for all ZnS:Mn samples, and the peak intensity reaches a maximum with a Mn content of 0.68 atom % from the EDX analysis in 2 atom % Mn-doped ZnS samples.



## 1. INTRODUCTION

The self-assembled nanostructures have attracted much attention due to a prospective wide range of technological applications in electronics, optics, biomedicine, and mechanics. The key aspects in nanotechnological processes include control growth of nanocrystal structures and self-assembled nanostructures within the building blocks of special nanodevices. Significant research efforts have been made to control the shapes of nanocrystals, such as nanotubes, nanowires, nanoribbons, nanosheets, and bundles. Several integrated nanostructures have been achieved, such as circuit networks, building blocks of nanoparticles, and nanowires.

Zinc sulfide, an important semiconductor compound of the IIB–VI groups, has a wide band-gap energy (3.77 eV) for the wurtzite (WZ, or  $2\text{H-ZnS}$ )<sup>1</sup> structure and 3.72 eV for the zinc-blende (ZB, or  $3\text{C-ZnS}$ )<sup>2</sup> structure at 300 K. It is a luminescent material well-known for its photoluminescence<sup>3</sup> and electroluminescence,<sup>4</sup> which enable wide applications in the fields of displays,<sup>5</sup> its photodetector,<sup>6</sup> sensors,<sup>7</sup> and lasers.<sup>8,9</sup> One-dimensional (1D) ZnS nanostructures, such as nanowires, nanobelts, nanocables, and nanotubes recently have been synthesized by several groups.<sup>10–16</sup> And there are some reports on the building blocks of ZnS nanostructures: Zhu et al.<sup>17</sup> synthesized ZnS–C nanocable heterostructures and nanocable-aligned ZnS tetrapods; Liu et al.<sup>18</sup> found that ZnS bicrystal structures are composed of two kinds of planes with only one atomic layer as the twin boundary; Hu et al.<sup>19</sup> achieved epitaxial semiconducting heterostructures (side-to-side Si–ZnS, Si–ZnSe biaxial nanowires, and sandwichlike ZnS–Si–ZnS triaxial nanowires), Wang et al.<sup>20</sup> reported epitaxial growth of ZnO nanowires on ZnS nanobelts by metal organic chemical vapor deposition; Zhang et al.<sup>21</sup> synthesized nano-ZnS with mixed cubic and hexagonal stacking; Lu et al.<sup>22</sup> and Yan et al.<sup>23</sup>

synthesized vertically aligned ZnO–ZnS heterojunction nanowire (NW) arrays; and Shen et al.<sup>24</sup> reported heteroepitaxial growth of orientation-ordered ZnS nanowire arrays. Recently, Bian et al.<sup>25</sup> reported on the nanocrystal superlattices assembled by colloidal PbS NCs with bcc and fcc symmetry, but until now there are no reports on the ZnS superlattice structures.

On the other hand, nanocrystalline transition metal-doped ZnS attracted much attention because properties in optics and magnetism differ significantly from those of their undoped counterparts. People have paid more attention to Mn-doped ZnS nanocrystals because the Mn-doped ZnS nanostructures have much better optical properties.<sup>26–30</sup>

In this paper, we report on the novel nanobelts composed of a hexagonal wurtzite structure and a zinc-blende structure ZnS atom layers. The structural relationship between the atom layers is thoroughly studied using high-resolution transmission electron microscopy (HRTEM) and selected area electron diffraction (SAED) techniques. The  $(3\text{C-ZnS})(111)/(2\text{H-ZnS})(001)$  superlattice structures have been investigated in Mn-doped ZnS nanoribbons, where the Mn-doped ZnS nanoribbons with a width of several hundred nanometers and a length of about tens to one hundred micrometers were prepared on Au-coated Si substrates by a chemical vapor transport method. To the best of our knowledge, this is the first report of  $(3\text{C-ZnS})(111)/(2\text{H-ZnS})(001)$  superlattice along the growth direction in the plane of the ZnS nanoribbon. And both the growth mechanism of the  $(3\text{C-ZnS})(111)/(2\text{H-ZnS})(001)$  superlattice structure and photoluminescence mechanism are

Received: August 24, 2012

Revised: October 16, 2012

Published: October 16, 2012



explained for the Mn-doped ZnS nanostructures. Those well-defined and composition-tunable ZnS nanostructures would be able to provide new building blocks for various optical devices and find applications in nanoelectronics and photonics.

## 2. EXPERIMENTAL SECTION

One-dimensional Mn-doped ZnS nanowires were synthesized in a horizontal tube furnace through a simple thermal evaporation process, as reported elsewhere.<sup>30</sup> For the synthesis of Mn-doped ZnS nanowires, a mixture of ZnS powder (0.30 g, 99.99%, Sigma-Aldrich) and MnCl<sub>2</sub> powder (0.002 g, 99.999%, Sigma-Aldrich) was placed in an alumina boat in the middle of the heating zone. A Si(100) substrate coated with a Au film was obliquely put downstream of ZnS powder at a distance of 15 cm. Before heating, the system was purged with 517 sccm (standard cubic centimeter per minute) high-purity argon (Ar 99.999%) for 15 min. Then, the pressure was reduced to  $7.5 \times 10^{-2}$  Torr for the duration of the reaction. After that, the furnace was heated with a heating rate of 10 °C/min to 1050 °C and kept at the temperature for 30 min with the Ar flow keeping at 50 sccm. After the system was cooled down to room temperature, a white-colored wool-like product was found deposited on the silicon substrate. In the same way, other Mn-doped ZnS nanowires with different masses of MnCl<sub>2</sub> powder (0.004 g, 0.008 g, 0.012 g, 0.020 g, and 0.040 g, respectively) were prepared, where the Mn-doping ratio in the synthesized ZnS:Mn samples was 0.5, 1, 2, 3, 5, and 10 atom %.

The as-synthesized products were characterized by X-ray diffraction (XRD-7000, Shimadzu) using Cu K $\alpha$  radiation ( $\lambda = 0.15406$  nm). The XRD data were collected with a scanning speed of 7° 2 $\theta$ /min in the 2 $\theta$  range from 10° to 65° by a continuum scanning method. The morphology and microstructure of the samples were observed by a field-emission scanning electron microscopy instrument (FESEM, s-4800II, Hitachi) equipped with an X-ray energy dispersive spectrometer (EDS) under an acceleration voltage of 15 kV and a high-resolution transmission electron microscope (HRTEM, Tecnai F30, FEI). The photoluminescence (PL) and absorption measurements were carried out by a luminescence spectrophotometer (PL, EPL-375, Edinburgh) and UV-vis-NIR spectrophotometer (UV-vis, Cary-5000, Varian), respectively.

## 3. RESULTS AND DISCUSSION

### 3.1. Structural Characterization and Morphology.

FESEM analysis exhibits that the as-synthesized products have similar morphologies with different Mn contents as shown in Figure 1, where Figure 1(panels a–f) are the images of ZnS:Mn nanocrystals with the raw Mn content equal to (a) 0.5, (b) 1, (c) 2, (d) 3, (e) 5, and (f) 10 atom %, respectively. The low-magnification FESEM images reveal that the products consist of a large quantity of flexible and wirelike nanostructures (as shown in the inset of Figure 1), and the high-magnification FESEM images show that they are all nanoribbons from different views. From Figure 1, one can find that all nanoribbons grow uniformly with the width of 100–800 nm, and the length of tens to more than one hundred micrometers and a Au nanodroplet can be found at the top of the as-synthesized products marked by a white circle, as shown in Figure 1h. Figure 1, panels a–f shows that the doping of Mn element has no effect on the morphology of the ZnS:Mn nanoribbons, since the amount of Mn obtained by EDX analysis in the ZnS nanoribbons doped with various Mn

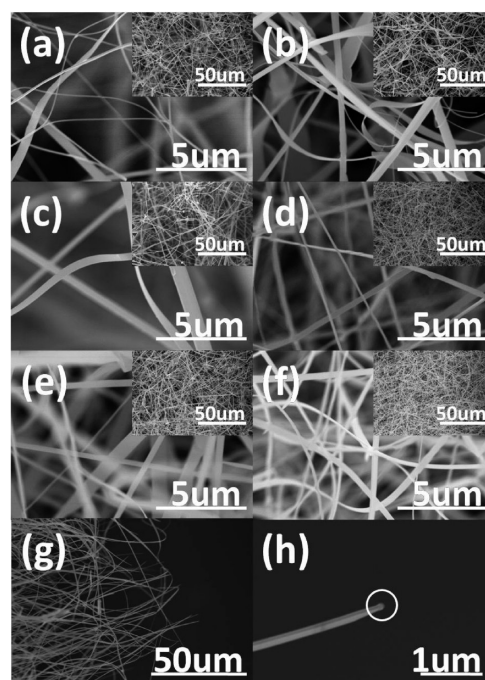


**Figure 1.** High-magnification SEM micrographs of the as-grown products and low magnification in the corresponding inset: (a) 0.5%, (b) 1%, (c) 2%, (d) 3%, (e) 5%, (f) 10%, and (g, h) the top of the ZnS nanoribbons.

contents (0.5, 1, 2, 3, 5, and 10 atom %) was 0.11–0.68 atom %, as shown in Table 1. Table 1 gives elemental quantitative

**Table 1. Element Quantitative Analysis of EDS Spectra for the Samples with Different Mn Content**

element	Mn content (%)	atom %
Mn	0.5	0.11
Mn	1	0.53
Mn	2	0.68
Mn	3	0.62
Mn	5	0.40
Mn	10	0.38

analysis of EDS spectra for the samples with different Mn contents. The amount of Mn obtained by EDX analysis in 0.5, 1, 2, 3, 5, and 10 atom percent-doped ZnS samples was an initial increase followed by a decrease with an increase in the content of raw Mn; it shows a maximum of 0.68 atom % when the Mn doping content is 2 atom %. It is hard to deposit a high ratio of Mn on the Au-coated substrate by using a thermal evaporation process; the reason needs to be clear.

Typical XRD patterns for ZnS:Mn nanoribbons doped with different Mn content are shown in Figure 2, where the standard spectra for the cubic and hexagonal ZnS are also presented for reference. It shows that the diffraction peaks of all the samples were almost identical with all the peaks representing the wurtzite phase of ZnS except that at  $2\theta = 32.9^\circ$  peculiar to the (200) plane of the zinc blende (JCPDS 65-0309), which matches well in the JCPDS (no. 36-1450) with a good crystalline quality with the lattice constants of  $a = 3.818$  Å and  $c = 6.259$  Å. The peak at  $2\theta = 32.9^\circ$  corresponds to the (200) plane of zinc blende (JCPDS 65-0309), and the [001] direction of the wurtzite ZnS structure is same as the [111] of the zinc-



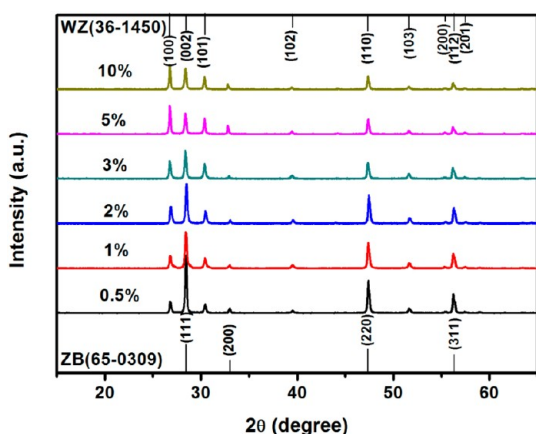


**Figure 2.** X-ray diffraction patterns of Mn-doped ZnS nanowires with different doping content [ $2\theta = 32.9^\circ$  peculiar to the (200) plane of zinc blende].

blende structure. Therefore, we conclude that both the wurtzite and the zinc-blende structures coexist in ZnS:Mn; this can be further confirmed by the HRTEM images. As the atomic ratios of Mn and Zn elements for all the ZnS:Mn nanoribbons are very close, the crystalline structures are almost identical as shown in Figure 2. Furthermore, there is no XRD peak related to Mn compounds in the Mn-doped ZnS nanoribbons. We believed that Mn elements have been doped into the ZnS lattice and have replaced the positions of Zn atoms. But, the Mn content will influence the crystalline directions of the samples; in a relatively low Mn-dopant content, the strong diffraction peak corresponds to the (002) diffraction plane. This means that the nanoribbons formed by two types of structures have the preferred [001] direction which is perpendicular to the axis direction of the ZnS:Mn nanoribbons, while at a relatively high Mn-dopant content, there is no strong main peak, and the preferred growth direction is not obvious.

The structure and morphology of the ZnS nanostructures can be investigated by the TEM, as shown in Figure 3: Figure 3 shows the bright-field TEM images of one nanoribbon of the Mn-doped ZnS (2%) with a width of 250 nm (as shown in Figure 3a); Figure 3b is the HRTEM image of the border of the cross section in the nanoribbon; the inset of Figure 3d shows the SAED patterns in Figure 3b; Figure 3, panels e and f are the HRTEM images of the middle of the cross section in the nanoribbon; and the inset of Figure 3f shows the corresponding SAED patterns in Figure 3e. From Figure 3d, the measured lattice fringes are 0.335 nm and 0.628 nm, which correspond to the {100} and {001} crystallographic plane of the wurtzite ZnS, respectively, as indicated in the XRD powder diffraction file (36-1450). For the two-sides nanoribbon, the lattice fringes and SAED patterns reveal that the growth directions of the samples are mainly along the [001] and [100] direction, and the ZnS crystal is a dislocation-free single-crystalline. For the middle of the ZnS nanoribbon, there is a central atom layer with a width of 3.03 nm, and two atom layers align separately along the central atom layer, as shown in Figure 3e. The HRTEM image of the two atom layers (in Figure 3f) shows that the marked interplanar  $d$  spacing ( $\sim 0.312$  nm) corresponds to that of the {111} lattice planes of the zinc-blende ZnS, and the widths of the two atom layers are 4.56 nm and 5.56 nm, respectively. The central atom layer has a hexagonal wurtzite structure and grows along the [100] axis direction and the [001] vertical direction. Also, there are two sets of diffraction spots as the inset of Figure

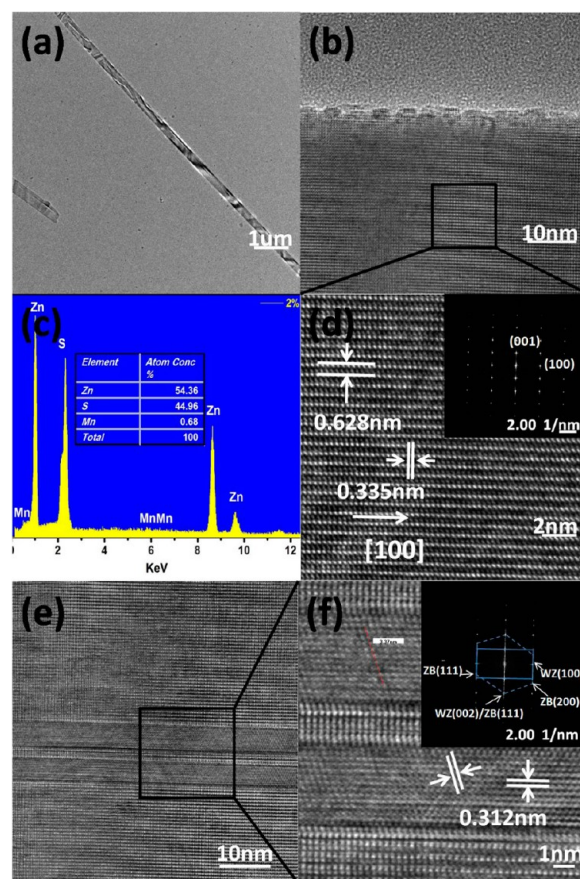


**Figure 3.** (a, b) TEM and (d) HR-TEM images and (c) EDS spectrum for Mn-doped (2%) ZnS nanoribbons. (e, f) HR-TEM images for the middle part of Mn-doped (2%) ZnS nanoribbons. The inset in the HR-TEM image is SAED.

3f; one is indexed to WZ ZnS, indicated by a rectangle, and the other is indexed to ZB ZnS, marked by a dashed hexagon. The HRTEM image shows that both the zinc-blende and wurtzite structure phases coexist in the ZnS:Mn nanoribbons, and the (001) plane of WZ ZnS are parallel to the (111) plane of the zinc-blende ZnS. Thus, the ZnS:Mn portion has the homocrystalline superlattice structure  $(3C\text{-ZnS})/(2H\text{-ZnS})$  [111]-[001]. The EDS spectrum of the Mn-doped ZnS nanoribbons (2%) indicates that Zn and S are major elements in Figure 3c; a small portion of the Mn element is observed where the atomic percentage of Mn is 0.68 atom %, far less than the 2% of the stoichiometric ratio of the raw material, and the atomic percentage of S is less than that of Zn.

The growth of the Mn-doped ZnS homocrystalline superlattice structure could be ascribed to the traditional vapor-liquid-solid mechanism.<sup>31</sup> According to the above, it is proposed that the growth of the Mn-doped ZnS homocrystalline superlattice structure can be divided into two steps, namely, preferred 1D growth and two-dimensional (2D) epitaxial growth vertical to the axis direction, as illustrated in Figure 4a. At a high temperature (1050 °C), ZnS vapor is produced quickly by evaporation of ZnS powder. Next, the ZnS vapor concentration surrounding the Au droplets on the Si substrates will increase; the absorption and precipitation of ZnS vapor processes were rapid. On the other hand, there are sufficient Au droplets on the Si substrate, and these Au droplets are likely to congregate in elliptical or linear shape under the reaction of Ar

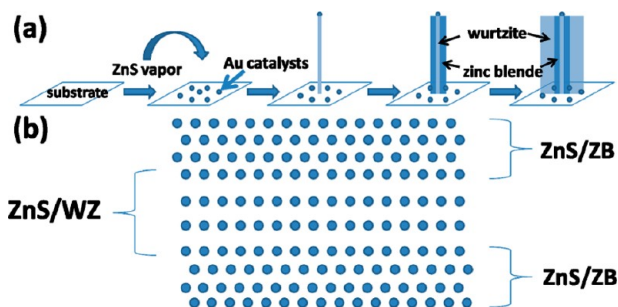


**Figure 4.** (a) Schematic illustration for the growth mechanism of the Mn-doped ZnS homocrystalline superlattice structure and (b) atomic layer accumulation.

carrier gas; those elliptical or linear Au droplets absorbed ZnS vapor quickly, resulting in the formation of very long nanoribbons, as discussed in reference 14. Because of the high temperature, the ZnS nanoribbon precipitates in a wurtzite structure with a preferential growth orientation. As mentioned above, the formation of the nanoribbon is related to the Au droplets with an elliptical or linear shape. The width of the nanoribbon is determined by the major axis of an ellipse; when the nanoribbon becomes wider, the strain will develop at the two sides of the central region, as shown in Figure 4b. Part of the atoms originally arrayed in the [001] direction of a wurtzite structure will align in the [111] direction of a zinc-blende structure, as their lattice fringes are close. Therefore, two separate atom layers with a zinc-blende structure are parallel to the central atom layer with a hexagonal structure. From the above analyses of the HRTEM images and growth process, the homocrystalline superlattice structure (3C-ZnS)/(2H-ZnS) [111]-[001] consists of various atom layers, and all the atom layers are in the plane of the ZnS:Mn nanoribbons.

Furthermore, a typical HRTEM image of 3 atom % Mn-doped ZnS nanoribbons was also investigated, and the magnified images of the ZnS:Mn nanoribbons show that there are alternative atom layers, which correspond to a wurtzite-structure ZnS grown along the [100] axis direction and the [001] vertical direction and a zinc-blende structure [111] direction in the ZnS:Mn nanoribbons. These results provide evidence for the formation of the ZnS superlattice, but a more detailed study must be done.

**3.2. Photoluminescence.** To examine the band gap and optical properties of the prepared ZnS nanoribbons with the change in Mn content, UV-vis absorption and PL spectra measurements were performed at room temperature, as shown in Figure 5. In the PL spectra shown in Figure 5a, three emission peaks at ~440 nm, ~520 nm, and ~580 nm in the UV-vis range are observed using an excitation wavelength of 325 nm in the prepared samples. A multipeak Gaussian fit gives four Gaussian bands, centering at ~440 nm, ~480 nm, ~515 nm, and ~580 nm, respectively. As shown in the inset of Figure 5a, the Gaussian curve fits well with the experimental curve. Therefore, the PL spectrum mainly consists of three emission bands at ~440 nm, ~480 nm, ~515 nm, and ~580 nm. The PL properties of Mn-doped ZnS nanostructures were extensively studied. The transfer of electrons and holes into the electronic level of the Mn ions induces the characteristic emission band around 580 nm, which is associated with the  $^4T_1$ - $^6A_1$  transition in  $Mn^{2+}$ .<sup>30,32,33</sup> Hence, the emission band around 580 nm for Mn-doped ZnS nanoribbons is attributed to  $Mn^{2+}$  dopants. The intensity of the emission peak centered at ~580 nm is the

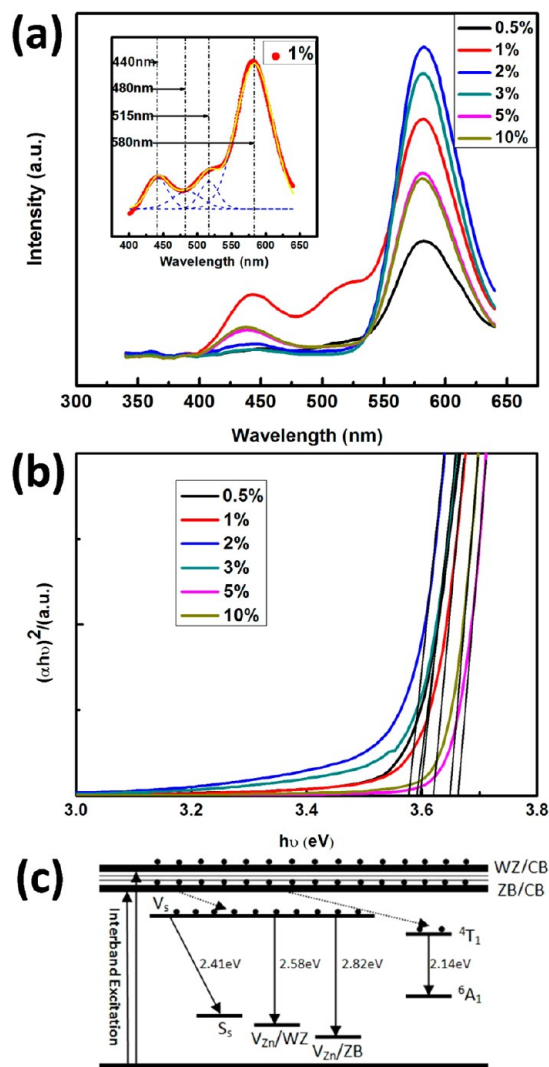


**Figure 5.** (a) PL and (b) UV-vis spectra of Mn doped with different doping content ZnS nanowires and (c) a schematic representation of the proposed mechanism for the PL excitation, the energy transfer, and the PL in Mn-doped ZnS nanoribbons.

strongest when the content of the Mn element is 2%. Because a cubic and a hexagonal structure coexists, the blue emission band centered at about ~440 nm may be attributed to the recombination of electrons from the conduction band with the holes from the energy level of zinc vacancies ( $V_{Zn}E$ ) of wurtzite-structured ZnS,<sup>12,34</sup> whereas the weak blue emission peak at ~480 nm may arise from the recombination of electrons from the conduction band with the holes from the energy level of zinc vacancies ( $V_{Zn}E$ ) of the zinc-blende-structured ZnS.<sup>35</sup> Moreover, the stable green emission band centered at ~520 nm was reported because of either the surface states<sup>36–38</sup> or the presence of Au.<sup>39</sup> Figure 5c shows a schematic representation of the proposed mechanism for the PL excitation and energy transfer. Also, Figure 5b shows the comparative UV-vis absorption spectra taken from the prepared samples. The absorption peak of Mn-doped ZnS nanoribbon is red shifted compared to that of the bulk ZnS. It is known that the relationship between the absorption coefficient ( $R$ ) near the absorption edge and the optical band gap ( $E_g$ ) for direct interband transitions obeys the following formula,<sup>40,41</sup>



$$(\alpha h\nu)^2 = A(h\nu - E_g) \quad (1)$$

where  $A$  is the parameter that relates to the effective masses associated with the valence and conduction bands, and  $h\nu$  is the photon energy. The optical absorption in the edge region can be well fitted by eq 1, as shown in Figure 5b, and the band gap of Mn-doped nanoribbons is from 3.58 to 3.68 eV. The red shift is connected with the doping of Mn element, and the variation of the band gap arose from the varying content of the Mn element.

To investigate the temperature dependence of the PL, we carried out integrated intensity measurements. The intensity of the emission band centered at 580 nm increases gradually with the decrease of the temperature, as shown in Figure 6. The

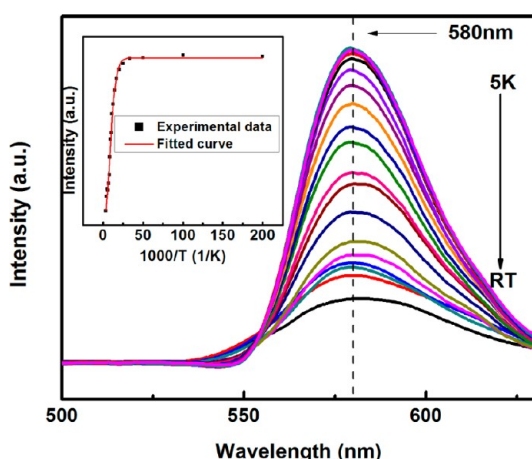


**Figure 6.** Temperature-dependent PL spectra of ZnS nanowires from 5 to 300 K; the inset displays the Arrhenius plot of the areal intensity of individual peaks centered at 580 nm with respect to the inverse temperature.

inset of Figure 6 displays an Arrhenius plot of the integrated PL intensity  $I(T)$  over the temperature range of 5–300 K for the emission band centered at 580 nm. The experimental data were fitted with the formula.<sup>42</sup>

$$I(T) = \frac{I(0)}{1 + C \exp(-E_a/KT)} \quad (2)$$

where  $I(0)$  is the integrated intensity at zero absolute temperature, and  $C$  is a constant. The solid lines in the inset of Figure 6 represent a simulation of the intensities using this theory. An activation energy of  $E_a = 23 \pm 1$  meV was obtained from the fitting. This value is in agreement with the previous reports<sup>43</sup> for the 580 nm emission peak in the  $\text{ZnS:Mn}^{2+}$  bulk. Excellent agreement between theory and experiment suggests that the intensity decrease of the emission is mainly due to thermal quenching. In general, quenching of luminescence with temperature can be explained by the thermal emission of carriers out of a confining potential with an activation energy correlated to the depth of the confining potential.<sup>44</sup> The activation energy of the emission band centered at 580 nm is much smaller than the delocalization energy; actually, it may be ascribed to the potential barrier for the electrons escaping from the  $^4T_1$  energy level to the  $^6A_1$  energy level, which was both the electronic levels of the  $\text{Mn}^{2+}$  ions and the giving off of energy by a nonradiative process.

## 4. CONCLUSION

In conclusion, Mn-doped ZnS nanoribbons have been successfully synthesized on Au-coated Si substrates by a chemical vapor transport method, where the individual Mn-doped ZnS nanoribbons have uniform widths ranging from 100 to 800 nm and lengths ranging from tens to one hundred micrometers. From the images of HRTEM and XRD, the successful growth of  $(3\text{C-ZnS})/(2\text{H-ZnS})$  superlattice structures in Mn-doped ZnS nanoribbons has been carried out, where a central atom layer with a width of 3.03 nm has a hexagonal wurtzite structure and grows along the  $[100]$  axis direction and the  $[001]$  vertical direction, and two atom layers with a zinc-blende structure growing along the  $\langle 111 \rangle$  direction align at both sides of the central atom layer. The formation of the ZnS superlattice may arise from the increase of the width and the high temperature. Four emission bands located at 440 nm, 480 nm, 515 nm, and 580 nm have been observed from the room temperature photoluminescence measurements, where the 440 and 480 nm blue emission bands are ascribed to the recombination of electrons from the conduction band with the holes from the energy level of zinc vacancies ( $V_{\text{Zn}}E$ ) of wurtzite and zinc-blende structured ZnS, respectively. For all ZnS:Mn samples, an identical strong photoluminescence transition centered at 580 nm has been observed with an activation energy of 23 meV. Those well-defined and composition-tunable ZnS nanostructures would be able to provide new building blocks for various optical devices and would be helpful to the applications in nanoelectronics and photonics.

## AUTHOR INFORMATION

### Corresponding Author

\*E-mail: xhzeng@yzu.edu.cn. Fax: +86 51487975467.

### Notes

The authors declare no competing financial interest.

## ACKNOWLEDGMENTS

The authors gratefully acknowledge the financial support for this work from Yangzhou Science and Technology Development (Grants YZ2010153 and YZ2011150).

## REFERENCES

- (1) Ong, H. C.; Chang, R. P. H. *Appl. Phys. Lett.* **2001**, 79, 3612–3614.
- (2) Tran, T. K.; Park, W.; Tong, W.; Kyi, M. M.; Wagner, B. K.; Summers, C. J. *J. Appl. Phys.* **1997**, 81, 2803–2809.
- (3) Zhao, Y. W.; Zhang, Y.; Zhu, H.; Hadjipianayis, G. C.; Xiao, J. Q. *J. Am. Chem. Soc.* **2004**, 126, 6874–6875.
- (4) Nakamura, S.; Yamada, Y.; Taguchi, T. *J. Cryst. Growth* **2000**, 214/215, 1091–1095.
- (5) Koutsogeorgis, D. C.; Mastio, E. A.; Cranton, W. M.; Thomas, C. B. *Thin Solid Films* **2001**, 383, 31–33.
- (6) Hu, L. F.; Yan, J.; Liao, M. Y.; Xiang, H. J.; Gong, X. G.; Zhang, L. D.; Fang, X. S. *Adv. Mater. (Weinheim, Ger.)* **2012**, 24, 2305–2309.
- (7) Fang, X. S.; Bando, Y.; Liao, M. Y.; Zhai, T. Y.; Gautam, U. K.; Li, L.; Koide, Y.; Golberg, D. *Adv. Funct. Mater.* **2010**, 20, 500–508.
- (8) Yan, H. Q.; He, R. R.; Johnson, J.; Law, M.; Saykally, R. J.; Yang, P. D. *J. Am. Chem. Soc.* **2003**, 125, 4728–4729.
- (9) Huang, M. H.; Mao, S.; Feick, H.; Yan, H. Q.; Wu, Y. Y.; Kind, H.; Weber, E.; Russo, R.; Yang, P. D. *Science* **2001**, 292, 1897–1899.
- (10) Shi, L.; Xu, Y. M.; Li, Q. *Cryst. Growth Des.* **2009**, 9, 2214–2219.
- (11) Banerjee, I. A.; Yu, L. T.; Matsui, H. *J. Am. Chem. Soc.* **2005**, 127, 16002–16003.
- (12) Chai, L. L.; Du, J.; Xiong, S. L.; Li, H. B.; Zhu, Y. C.; Qian, Y. T. *J. Phys. Chem. C* **2007**, 111, 12658–12662.

- (13) Liang, C. H.; Shimizu, Y.; Sasaki, T.; Umehara, H.; Koshizaki, N. *J. Phys. Chem. B* **2004**, *108*, 9728–9733.
- (14) Kar, S.; Chaudhuri, S. *J. Phys. Chem. B* **2005**, *109*, 3298–3302.
- (15) Fang, X. S.; Bando, Y.; Ye, C. H.; Shen, G. Z.; Golberg, D. *J. Phys. Chem. C* **2007**, *111*, 8469–8474.
- (16) Lu, J. F.; Zeng, X. H.; Liu, H. F.; Zhang, W.; Zhang, Y. *Appl. Surf. Sci.* **2012**, *258*, 8538–8541.
- (17) Zhu, Y. C.; Bando, Y.; Xue, D. F.; Golberg, D. *J. Am. Chem. Soc.* **2003**, *125*, 16196–16197.
- (18) Liu, B. D.; Bando, Y.; Liao, M. Y.; Tang, C. C.; Mitome, M.; Golberg, D. *Cryst. Growth Des.* **2009**, *9*, 2790–2793.
- (19) Hu, J. Q.; Bando, Y.; Liu, Z. W.; Sekiguchi, T.; Golberg, D.; Zhan, J. H. *J. Am. Chem. Soc.* **2003**, *125*, 11306–11313.
- (20) Wang, Z. Q.; Liu, X. D.; Gong, J. F.; Huang, H. B.; Gu, S. L.; Yang, S. G. *Cryst. Growth Des.* **2008**, *8*, 3911–3913.
- (21) Zhang, H. Z.; Banfield, J. F. *J. Phys. Chem. C* **2009**, *113*, 9681–9687.
- (22) Lu, M.-Y.; Song, J. H.; Lu, M.-P.; Lee, C.-Y.; Chen, L.-J.; Wang, Z. L. *ACS Nano* **2009**, *3*, 357–362.
- (23) Yan, J.; Fang, X. S.; Zhang, L. D.; Bando, Y.; Gautam, U. K.; Dierre, B.; Sekiguchi, T.; Golberg, D. *Nano Lett.* **2008**, *8*, 2794–2799.
- (24) Shen, G. Z.; Bando, Y.; Golberg, D.; Zhou, C. W. *J. Phys. Chem. C* **2008**, *112*, 12299–12303.
- (25) Bian, K.; Wang, Z. W.; Hanrath, T. *J. Am. Chem. Soc.* **2012**, *134*, 10787–10790.
- (26) Chung, J. H.; Ah, C. S.; Jang, D. J. *J. Phys. Chem. B* **2001**, *105*, 4128–4132.
- (27) Ren, H. B.; Wu, B. Y.; Chen, J. T.; Yan, X. P. *Anal. Chem.* **2011**, *83*, 8239–8244.
- (28) Zheng, J. J.; Yuan, X.; Ikezawa, M.; Jing, P. T.; Liu, X. Y.; Zheng, Z. H.; Kong, X. G.; Zhao, J. L.; Masumoto, Y. *J. Phys. Chem. C* **2009**, *113*, 16969–16974.
- (29) Quan, Z. W.; Wang, Z. L.; Yang, P. P.; Lin, J.; Fang, J. Y. *Inorg. Chem.* **2007**, *46*, 1354–1360.
- (30) Kang, T.; Sung, J.; Shim, W.; Moon, H.; Cho, J.; Jo, Y.; Lee, W.; Kim, B. *J. Phys. Chem. C* **2009**, *113*, 5352–5357.
- (31) Wagner, R. S.; Ellis, W. C. *Appl. Phys. Lett.* **1964**, *4*, 89–90.
- (32) Jung, D. R.; Son, D.; Kim, J.; Kim, C.; Park, B. *Appl. Phys. Lett.* **2008**, *93*, 163118.
- (33) Li, Y. Q.; Zapien, J. A.; Shan, Y. Y.; Liu, Y. K.; Lee, S. T. *Appl. Phys. Lett.* **2006**, *88*, 013115.
- (34) Hu, P. A.; Liu, Y. Q.; Fu, L.; Cao, L. C.; Zhu, D. B. *J. Phys. Chem. B* **2004**, *108*, 936–938.
- (35) Zhang, W. H.; Shi, J. L.; Chen, H. R.; Hua, Z. L.; Yan, D. S. *Chem. Mater.* **2001**, *13*, 648–654.
- (36) Ye, C. H.; Fang, X. S.; Wang, M.; Zhang, L. D. *J. Appl. Phys.* **2004**, *99*, 063504.
- (37) Ye, C. H.; Fang, X. S.; Li, G. H.; Zhang, L. D. *Appl. Phys. Lett.* **2004**, *85*, 3035–3037.
- (38) Tsuruoka, T.; Liang, C. H.; Terabe, K.; Hasegawa, T. *Appl. Phys. Lett.* **2008**, *92*, 091908.
- (39) Liang, C. H.; Shimizu, Y.; Sasaki, T.; Umehara, H.; Koshizaki, N. *J. Phys. Chem. B* **2004**, *108*, 9728–9733.
- (40) Li, L.; Yang, Y. W.; Huang, X. H.; Li, G. H.; Zhang, L. D. *J. Phys. Chem. B* **2005**, *109*, 12394–12398.
- (41) Li, L.; Yang, Y. W.; Li, G. H.; Zhang, L. D. *Small* **2006**, *2*, 548–553.
- (42) Ogino, T.; Aoki, M. *Jpn. J. Appl. Phys.* **1980**, *19*, 2395–2405.
- (43) Chen, W.; Su, F.; Li, G.; Joly, A. G.; Malm, J. O.; Bovin, J. O. *J. Appl. Phys.* **2002**, *92*, 1950–1955.
- (44) Makino, T.; Tamura, K.; Chia, C. H.; Segawa, Y.; Kawasaki, M.; Ohtomo, A.; Koinuma, H. *J. Appl. Phys.* **2003**, *93*, 5929–5933.